



**HAL**  
open science

# Thermodynamic Assessment of the Fe-Te System. Part II Thermodynamic modelling

C.-M. Arvhult, C. Guéneau, S. Gossé, . Selleby M

► **To cite this version:**

C.-M. Arvhult, C. Guéneau, S. Gossé, . Selleby M. Thermodynamic Assessment of the Fe-Te System. Part II Thermodynamic modelling. *Journal of Alloys and Compounds*, 2018, 767, pp.883-893. 10.1016/j.jallcom.2018.07.051 . cea-02339843

**HAL Id: cea-02339843**

**<https://cea.hal.science/cea-02339843v1>**

Submitted on 5 Nov 2019

**HAL** is a multi-disciplinary open access archive for the deposit and dissemination of scientific research documents, whether they are published or not. The documents may come from teaching and research institutions in France or abroad, or from public or private research centers.

L'archive ouverte pluridisciplinaire **HAL**, est destinée au dépôt et à la diffusion de documents scientifiques de niveau recherche, publiés ou non, émanant des établissements d'enseignement et de recherche français ou étrangers, des laboratoires publics ou privés.

# Thermodynamic Assessment of the Fe-Te System. Part II: Thermodynamic modelling

C.-M. Arvhult<sup>a</sup>, C. Guéneau<sup>b</sup>, S. Gossé<sup>b</sup>, M. Selleby<sup>a</sup>

<sup>a</sup> KTH Royal Institute of Technology, ITM, Dept. of Materials Science and Engineering, Unit of Structures, Brinellvägen 23, SE-100 44 Stockholm, Sweden

<sup>b</sup> Den-SERVICE de Corrosion et du Comportement des Matériaux dans leur Environnement (SCCME), CEA, Université Paris-Saclay, F-91191 Gif-sur-Yvette, France

Corresponding author: [arvhult@kth.se](mailto:arvhult@kth.se)

## Abstract

A thermodynamic description of the Fe-Te system modeled via the Calphad method is proposed, based on data published in a preceding publication *Part I: Experimental study*, and that available in literature. End-member formation energies for the phases  $\beta$ ,  $\beta'$ ,  $\delta$ ,  $\delta'$  and  $\epsilon$ , as well as lattice stabilities of FCC and BCC tellurium, have been evaluated via DFT and used in the numerical optimization. The final Gibbs energy models fit thermodynamic and phase diagram data well, and inconsistencies are discussed. The thermodynamic description is then used to evaluate Gibbs energy of formation for selected Fe-Te compounds of interest for the modeling of internal corrosion of stainless steel fuel pin cladding during operation of Liquid Metal-cooled Fast Reactors (LMFR).

*Keywords:* “nuclear reactor materials”, “interstitial alloys”, “thermodynamic modeling”, “thermochemistry”, “phase diagrams”, “phase transitions”

## 1. Introduction

In our preceding paper, *Part I: Experimental study*, we introduced the need of developing a thermodynamic description of the Fe-Te system for the modeling of internal corrosion in Generation IV nuclear reactors. The phase diagram of the system was updated with additional phase boundary data.

The present paper describes the thermodynamic assessment of the Fe-Te system based on the data acquired in *Part I: Experimental study*, and that available in the literature. An introduction to the phase diagram data and crystallographic data available in literature has already been presented in *Part I*. A brief review of available thermodynamic and thermochemical data follows in the next section.

## 2. State of the art on thermodynamic data of the Fe-Te system

Table 1 summarizes thermodynamic experimental data available in the literature for the Fe-Te system. Chemical potential and thermodynamic activity data have been evaluated via Electromotive Force (EMF) measurements [1], Knudsen effusion with mass-spectrometry and mass-loss techniques [2-4], torsion effusion [5] and isopiestic experiments [6]. Enthalpy measurements have been performed in the  $\beta$  and  $\beta+\epsilon$  regions [7-9]. Heat capacities have been measured on the  $\beta$  and  $\epsilon$  phases [10-12]. No enthalpy or heat capacity data are available for the  $\delta$  and  $\delta'$  phases.

Table 1: Summary of thermodynamic data available in literature for the Fe-Te system. \*: In the work by Geiderikh et al., the  $\delta$  and  $\delta'$  phases were not distinguished. \*\*: The data by Fabre interpreted correctly by Wagman et al. \*\*\*: Could not be acquired.

Phase(s)	Quantity	Experimental method(s)	T [K]	at.% Te	Reference(s)
Liquid	$a_{Te}$	Isopiestic	1077-1125	53.83-58.13	[6]
	$H_m^{E,\infty}$	Calorimeter	741	97.9	[13]
$\beta'$ -Fe <sub>1.12</sub> Te	$a_{Te}$	Isopiestic	1101-1140	46.12-47.47	[6]
$\beta$ -Fe <sub>1.11</sub> Te	$a_{Te}$	Isopiestic	971-1110	46.26-47.68	[6]
	$C_p$	Cryostat, DSC, Pulse Cal.	4.9-905	47.37	[10-12]
	$H_{for}^{298}$	Solution-Calorimeter	298.15	47.37	[8]
	$P_{Te_2}$	Torsion-Effusion	753-1106	45.95, 48.45	[5]
$\delta$ -Fe <sub>0.75</sub> Te	$a_{Te}$	Isopiestic	932-1080	55.79-58.35	[6]
$\delta'$ -Fe <sub>0.67</sub> Te	$a_{Te}$	Isopiestic	843-996	59.98-65	[6]
$\epsilon$ -FeTe <sub>2</sub>	$a_{Te}$	Isopiestic	904-906	67.55-67.62	[6]
	$C_p$	Cryostat, DSC	6.8-805	67.6	[10,11]
	$\mu_{Fe}$	EMF (Molten galv. cell)	650-880	66.2, 66.8	[1]
$\beta + \epsilon$	$H_{for}^{298}$	Calorimeter	298.15	59.10-62.11	[9]
	$H_{for}^{298}$	Solution-Calorimeter	298.15	50.05	[7,14]**
	$P_{Te_2}$	Knuds. Mass-Spectr. <sup>1</sup>	659-759		[3]
	$P_{Te_3}$	Knuds. Mass-Spectr.	699-759		[3]
	$\mu_{Fe}$	EMF (Molten galv. cell)	690-786	49-65	[1]
	$\beta + \delta$	$P_{Te_2}$	Knuds. Mass-Spectr.	868	
$P_{Te_3}$		Knuds. Mass-Spectr.	868		[3]
$P_{Te_2}$		Knuds. Mass-Spectr.	873-1023	50.05	[15]***
$\mu_{Fe}^*$		EMF (Molten galv. cell)	786-900	49-57	[1]
$\beta + \delta'$	$P_{Te_2}$	Knuds. Mass-Spectr.	803-818		[3]
	$P_{Te_3}$	Knuds. Mass-Spectr.	803-818		[3]
	$\mu_{Fe}^*$	EMF (Molten galv. cell)	786-900	49-57	[1]
$\alpha$ -Fe + $\beta$	$P_{Te}$	Knuds. Mass-Spectr.	901-1048	<47.3	[2]
	$P_{Te_2}$	Knuds. Mass-Spectr.	885-1048	<47.3	[2]
	$P_{Te_2}$	Knuds. Mass-Spectr.	866-999	<46	[4]

The formation enthalpy of  $FeTe_{0.9}$   $\beta$  phase calculated by Wagman et al. [14] from the measurements by Fabre [7] is unreasonably low ( $-62.7 \text{ kJ/mol}$ ), many times lower than that of Shukla et al. ( $-23.46 \text{ kJ/mol}$ ) [8], and is probably incorrect. The excess enthalpy of solution for infinite dilution of Fe in Te by Maekawa and Yokokawa [13] was comparatively low, but the brevity of their paper makes it difficult to evaluate. Vladimirova et al. [9] noted in their calorimetric study of  $\beta + \epsilon$  samples that an extrapolation from the expected formation enthalpy of  $\beta$ , which was consistent with the measurement by Shukla et al., through their two-phase data points resulted in a much lower formation enthalpy of the  $\epsilon$  phase than the value derived from Geiderikh et al. [1]. This must be carefully regarded when optimizing the system. Mikler et al. [11] noted an anomalous

<sup>1</sup> Mass-Spectrometry with Knudsen-Effusion.

increase in heat capacity in their measurement on the  $\epsilon$  phase; while they cannot explain it, they suggest that perhaps pure tellurium was precipitated during the measurement. This is possible since the solubility limits were not well known at the time; with an updated suggested phase boundary from the experimental results obtained in *Part I: Experimental study*, an explanation will be suggested in order to decide whether or not this increase should be modeled. Most activity and partial pressure measurements (Table 1) are consistent, however the partial pressure measurements by Romyantsev et al. [15] was found to be inconsistent with the isopiestic work by Ipser et al. [6], motivating the work by Prasad et al. [4]. They conclude that in an operating fast reactor with ASTM 316 stainless steel cladding the tendency of telluride formation will be  $\text{Cr} > \text{Fe} > \text{Ni}$ , i.e. the chromium tellurides are the most stable, and nickel tellurides the least.

Based on the available literature at hand, together with the new phase diagram data obtained in *Part I*, this work presents a thermodynamic assessment of the Fe-Te system performed via the Calphad method. To assist the numerical optimization, Density Functional Theory (DFT) calculations were performed to evaluate the formation enthalpy of the  $\epsilon$  phase discussed above, as well as the other intermediate phases. After covering those two methodologies in Sections 3 and 4, the numerical optimization procedure is detailed in Section 5. The results of the DFT calculations in Section 6 is followed by the final phase diagram of the system in Section 7. Finally, Section 8 concludes with suggestions for future studies.

### 3. DFT methodology

The density functional theory calculations of the total energies have been performed by means of the projector-augmented wave (PAW) method [16,17] as implemented in the Vienna ab initio simulation package (VASP) [18-21]. Exchange- correlation effects have been treated in the framework of the generalized gradient approximation (GGA) using the parametrization by Perdew, Burke, and Ernzerhof (PBE) [22,23]. The cutoff energy and k-points were converged, followed by volume optimization by minimizing the total energy via lattice parameter variation. Phases with internal degrees of freedom, e.g.  $c/a$  and  $b/a$  ratios different from unity, had those degrees of freedom optimized by shape relaxation. Terminal phase models were validated by comparing the relaxed lattice parameters, final magnetism and bulk modulus with experimental values, and checking if the density of states (DOS) is reasonable. The bulk moduli were calculated via the elastic tensor, obtained by displacing each ion of a structure in every direction and calculating the Hessian matrix. Table 2 shows chosen input and converged parameters for the elements. For hexagonal and pseudo-hexagonal phases a  $\Gamma$ -centered k-point grid was used; for cubic phases, Monkhorst-Pack meshes were used; for other structures, k-point distributions were automatically generated by VASP.

Table 2: DFT model input and converged parameters for tellurium and iron

Element	Stable phase	Potential used	Valence $e^-$	Conv. $E_{cutoff}$ [eV]	Conv. K-points	$V_{rel}$ [ $\text{\AA}^3$ ] (ref)	$K_V^2$ [GPa]	$K_{exp}$ [GPa]
Fe	BCC_A2	GGA_GW 2010	$3d^7 4s^1$	450	22x22x22	22.63 (23.7)	202.2	166.33 [24]
Te	A8 Hexagonal	GGA_GW 2012	$5s^2 5p^4$	330	19x19x15	104.9 (101.8)	20.3	27.34 <sup>3</sup> [25]

The lattice stabilities of FCC and BCC tellurium were evaluated, as well as the energy of formation of the compounds  $\beta\text{-Fe}_2\text{Te}$ ,  $\beta\text{-FeTe}$ ,  $\beta'\text{-Fe}_3\text{Te}_2$ ,  $\delta\text{-FeTe}$ ,  $\delta\text{-FeTe}_2$ ,  $\delta\text{-Fe}_3\text{Te}_4$ ,  $\delta'\text{-FeTe}$ ,  $\delta'\text{-FeTe}_2$ ,  $\delta''\text{-Fe}_2\text{Te}$ ,  $\varepsilon\text{-FeTe}_2$  and  $\varepsilon\text{-Te}_2$ . The formation energy of a compound,  $\text{Fe}_a\text{Te}_b$ , at 0 K was calculated as

$$\Delta E^{Fe_aTe_b} = E^{Fe_aTe_b} - aE_{Fe}^{BCC} - bE_{Te}^{A8} \quad \#(1)$$

where a and b are the stoichiometric coefficients of the phase under consideration, and the reference energies  $E_{Fe}^{BCC}$  and  $E_{Te}^{A8}$  are calculated at the same cutoff energy as  $E^{Fe_aTe_b}$  (i.e. those in Table 4). In particular, the ground state of  $\delta\text{-FeTe}$  was calculated in different space groups, while it was kept in mind that 0 K-calculations will not accurately predict the stable space group of a high-temperature phase, but merely give an idea. The meaning of calculating the formation energy of hypothetical compounds will be further explained in section 4.

<sup>2</sup> Voigt average bulk modulus, calculated from the 6x6 elastic tensor as

$$K_V = \{C_{11} + C_{22} + C_{33} + 2 \cdot (C_{12} + C_{13} + C_{23})\}/9$$

<sup>3</sup> Voigt average bulk modulus calculated from experimentally determined elastic tensor coefficients

## 4. Calphad methodology

The Compound Energy Formalism (CEF) and the Calphad method, described in the literature [26,27], were used for the thermodynamic assessment of the system. Using the CEF, a solution phase is modeled by dividing a crystal structure into sublattices representing their unique crystallographic sites. Gibbs energy is a surface stretched out between end-point compositions represented by all sublattices fully occupied by a single constituent. These are called end-members, and are either stable compositions, e.g.  $\epsilon\text{-FeTe}_2$ , or hypothetical compounds, e.g.  $\delta'\text{-FeTe}_2$ . The individual sublattice models of the phases are further detailed in paragraphs 4.1-4.2.

The molar Gibbs energy of a phase  $\alpha$  is expressed using the CEF as

$$G_m^\alpha = {}^{srf}G_m^\alpha + {}^{cnf}G_m^\alpha + {}^E G_m^\alpha + {}^{phys}G_m^\alpha \quad \#(2)$$

$${}^{srf}G_m^\alpha = \sum_{I_0} P_{I_0}(Y) {}^\circ G_{I_0} \quad \#(3)$$

$${}^{cnf}G_m^\alpha = RT \sum_{s=1}^n a_s \sum_{i=1}^{n_s} y_i^{(s)} \ln(y_i^{(s)}) \quad \#(4)$$

$${}^E G_m^\alpha = \sum_{I_1} P_{I_1}(Y) L_{I_1} + \sum_{I_2} P_{I_2}(Y) L_{I_2} + \dots \quad \#(5)$$

where  ${}^{srf}G_m^\alpha$  is the surface of reference energy, a contribution of hypothetical mechanical mixing of the pure constituents.  $I_0$  is a constituent array, of zeroth order, describing an end-member compound with a constituent in each sublattice,  $P_{I_0}$  is the product of those constituent fractions, and  ${}^\circ G_{I_0}$  is the Gibbs energy of formation of that end-member.  ${}^{cnf}G_m^\alpha$  is the configurational entropy of random mixing of the constituents  $y_i^{(s)}$ , with  $a_s$  as the number of sites per sublattice.  ${}^E G_m^\alpha$  is the excess Gibbs energy from interaction between constituents on a sublattice, where  $L_{I_1}$  is the interaction parameter for a first-order constituent array  $I_1$ , i.e. an extra constituent on the sublattice, where again  $P_{I_1}$  is the product of the regarded constituent fractions. The second-order parameter  $L_{I_2}$  regards interaction of constituents on two sublattices; use of higher-order parameters than the second is uncommon, and only the first will be used here.  ${}^{phys}G_m^\alpha$  represents other physical contributions, e.g. by magnetism.

### 4.1. Solution phases

Table 3 summarizes the sublattice models chosen for the modeling of the Fe-Te system, as well as the resulting end-members. For a table of the crystal structures of the system, see *Part I: Experimental Study*.

The  $\beta\text{-Fe}_{1.11}\text{Te}$  phase was modeled with three sublattices as  $(\text{Fe})_1(\text{Te})_1(\text{Fe,Va})_1$ , the first sublattice representing the tetrahedral holes in the tellurium lattice with fixed iron occupation, and the third iron sublattice representing the partially occupied octahedral holes with vacancy defects; it should be noted that at lower temperature, magnetic ordering gives rise to a monoclinic structure (Fe-rich side) and an orthorhombic structure (Te-rich side) [28], structures which will not be modeled here since the scope of this paper is higher temperatures.

The  $\epsilon\text{-FeTe}_2$  phase was modeled as the marcasite structure, with vacancy defects randomly distributed on the iron sublattice as  $(\text{Fe,Va})_3(\text{Te})_2$ . The  $\beta'\text{-Fe}_{1.12}\text{Te}$  phase was modeled in a similar way as  $(\text{Fe,Va})_3(\text{Te})_2$  according to the crystal structure  $\text{Fe}_{0.28}\text{Ni}_{0.28}\text{Te}_{0.44}$  [29]. The  $\gamma$  phase was

modeled as stoichiometric via  $(\text{Fe})_1(\text{Te})_{1.183}$  according to the composition 54.2 at% Te suggested by Ipsier et al. [30].

Different models were tested for the NiAs-type phases, i.e.  $\delta$  and  $\delta'$ , that tend to behave differently in different chemical systems. The greatest question was how to model monoclinic  $\delta$  phase, and whether it is disordered like the NiAs structure, or ordered in layers similar to the  $\text{CdI}_2$ -structure. An important comparison is with the same phase in the Ni-Te system, where it experiences a 2<sup>nd</sup> order NiAs to  $\text{CdI}_2$ -type transition resulting in a maximum in the  $c$  lattice parameter at 54 at% Te, which was not found at the  $\delta - \delta'$  transition in the Fe-Te system. In order to facilitate future compatibility with the Ni-Te system, it was eventually chosen to model them as one ordered phase with a miscibility gap, with one composition set representing  $\delta\text{-Fe}_{0.75}\text{Te}$  and one representing  $\delta'\text{-Fe}_{0.67}\text{Te}$ , described as  $(\text{Fe},\text{Va})_1(\text{Fe},\text{Va})_1(\text{Va})_2(\text{Te})_2$ . The first sublattice represents the 1a octagonal interstitial site in the  $\text{CdI}_2$  structure, being fully occupied in  $\text{CdI}_2$  but partially so in NiAs. The second sublattice represents the 1b position, having the same random occupation as 1a in the NiAs structure. The third sublattice, which is optional – and hereafter omitted – may be added to accommodate for the possibility of including interstitial atoms in the trigonal-bipyramidal sites, as is possible e.g. with Sn in the Ni-Sn-Te system, among others [31].

If heat capacity data is available, the end-member energies of phases are described with a power series in temperature, here expressed for a generic compound  $\text{A}_i\text{B}_j$

$$\Delta^o G_m^{A_i B_j} = {}^o G_m^{A_i B_j} - H_m^{SER} = a + bT + cT \ln(T) + dT^2 + eT^{-1} + fT^3 \#(6)$$

Since absolute values of Gibbs energy are meaningless, one always expresses numerical values relative to a reference state, here  $H_{SER}$ , the Standard Element Reference, is the enthalpy of the stable state at 1 bar of pressure and room temperature. If there is no  $C_p$  data available for a phase, it is common to approximate it with a weighted average of  $C_p$  of the pure elements, i.e. the Neumann-Kopp rule (NKR). In Calphad it is common to instead use a linear combination of Gibbs energy of the pure components, according to

$$\Delta^o G_m^{A_i B_j} - (i^o G_A + j^o G_B) = a + bT \#(7)$$

which is equivalent to the Neumann-Kopp rule.

## 4.2. Liquid phase

The liquid was initially modeled as a substitutional solution (Fe,Te) – however, it proved difficult to obtain the evidently steep iron-rich liquidus previously noted [30]. In order to accommodate for the possibility that this may be due to the presence of a liquid miscibility gap in the range Fe-FeTe at high temperature, as well as facilitate the future addition of oxygen to the system, the liquid was modeled with the partially ionic two-sublattice liquid model [32] with a neutral FeTe associate in the anion sublattice, as  $(\text{Fe}^{+2})_p(\text{Va}^{-Q}, \text{Te}^0, \text{FeTe}^0)_Q$ .  $P$  and  $Q$  are equal to the average charge of the respective opposite sublattice in order to maintain charge neutrality, i.e. here  $Q = 2$  and  $P = Q \cdot y_{Va}''$ . In the binary system this model is also equivalent to a solution model with an associate, (Fe,FeTe,Te). The Gibbs energy description of this model [27] is different from that of Equation 3 through 5, instead expressed as Equations 8 through 10:

$${}^{srf}G_m^{liq} = Q(y'_{Fe^{+2}}y''_{Va^{-2}}{}^{\circ}G_{Fe^{+2},Va^{-2}} + y''_{Te^0}{}^{\circ}G_{Te^0} + y''_{FeTe^0}{}^{\circ}G_{FeTe^0}) \#(8)$$

$${}^{cnf}G_m^{liq} = QRT[y''_{Va^{-2}} \ln(y''_{Va^{-2}}) + y''_{Te^0} \ln(y''_{Te^0}) + y''_{FeTe^0} \ln(y''_{FeTe^0})] \#(9)$$

$${}^E G_m^{liq} = Qy'_{Fe^{+2}}y''_{Va^{-2}}y''_{Te^0}L_{Fe^{+2},Va^{-2},Te^0} + Qy''_{Va^{-2}}y''_{FeTe^0}L_{Fe^{+2},Va^{-2},FeTe^0} + y'_{Fe^{+2}}y''_{FeTe^0}y''_{Te^0}L_{Fe^{+2},FeTe^0,Te^0} \#(10)$$

Here,  $y'_{Fe^{+2}}$  is always equal to unity since it is the sole cation occupying the first sublattice, but it remains in the equations for clarity.

Table 3: Sublattice models used for solution phases of the Fe-Te system. The gas phase is taken from the SGTE SSUB5 [33-35] database. Fe (FCC and BCC) phases and Te (A8) are taken from the SGTE PURE5 database [36].

Phase	Sublattice model	End-members	Range at.% Te	Comment
Liquid	$(Fe^{+2})_p(Va^{-Q}, FeTe^0, Te^0)_Q$	$Fe^{2+}_2, FeTe^0_2, Te^0_2$	0-100	
$\alpha$ -Fe	$(Fe, Te)_1(Va)_3$	$Fe_1Va_3, Te_1Va_3$	0-100	
$\gamma$ -Fe	$(Fe, Te)_1(Va)_1$	$Fe_1Va_1, Te_1Va_1$	0-100	Ideal solution
$\beta'$	$(Fe, Va)_3(Te)_2$	$Fe_3Te_2, Va_3Te_2$	40-100	
$\beta$	$(Fe)_1(Fe, Va)_1(Te)_1$	$Fe_1Fe_1Te_1, Fe_1Va_1Te_1$	33.33-50	
$\gamma$	$(Fe)_1(Te)_{1.183}$	$Fe_1Te_{1.183}$	54.2	
$\delta/\delta'$	$(Fe, Va)_1(Fe, Va)_1(Te)_2$	$Fe_1Fe_1Te_2, Fe_1Va_1Te_2, Va_1Fe_1Te_2, Va_1Va_1Te_2$	50-100	$Fe_1Va_1Te_2$ and $Va_1Fe_1Te_2$ are equivalent
$\epsilon$	$(Fe, Va)_1(Te)_2$	$Fe_1Te_2, Va_1Te_2$	66.67-100	

## 5. Optimization procedure

The thermodynamic assessment was performed using the PARROT module of the Thermo-Calc software package [37]. All intermediate phases were initially modeled as stoichiometric in order to obtain an initial description of the liquid phase. The liquid interaction parameters were fitted to isopiestic activity and liquidus data. Solid solution phases were then introduced. The phase diagram was found challenging to model, and the phases were introduced and optimized one by one in many different orders before coming to the following procedure, which was successful.

### 5.1. Liquid and terminal phases

The liquid model parameters were first adjusted to create a miscibility gap in the Fe-FeTe range, then optimized to fit liquidus data [30,38] and the steep liquidus found via DTA in the preceding experimental work (Fig. 4 in *Part I: Experimental study*). The  ${}^0L_{Fe^{+2},Va,Te}$  parameter was fixed to  $50 \cdot T$  in order to suppress a mixture of Fe and Te, i.e. promote the  $FeTe^0$  associate in the liquid, without producing an inverse miscibility gap.

A regular solution parameter was added to the  $\alpha$ -Fe phase and optimized to fit the solubility limits found in the experimental study of *Part I* and the tie-line of Ipsier et al. [30]. Te was added to the iron sublattice of  $\gamma$ -Fe to introduce the lattice stability evaluated in this work; the phase was otherwise not optimized. Iron was not added to pure Te, since its solubility has been previously found to be very small [30].



## 5.2. $\beta$ and $\epsilon$ phases

The  $c$ ,  $d$  and  $e$  parameters (in Eq. 6) of the  $\beta$ - $FeTe$  and  $\epsilon$ - $FeTe_2$  end-members were fitted to the available  $C_p$  data [10,11]. The  $a$  parameters for the  $\beta$  phase were then fitted to enthalpy of formation by Shukla et al. [8] and the  $\beta$ - $Fe_2Te$  end-member formation energy evaluated in this work. The  $a$  parameter of the  $\epsilon$  phase was fitted to derived formation enthalpy data [1]. The  $b$  terms of the end-members were then adjusted to obtain a reasonable melting temperature, then fitting interaction parameters to isopiestic activity data [6]. The remaining intermediate phases could then be introduced. All activity data sets were fitted by first introducing a regular solution parameter (Eq. (5)). Then the temperature-dependent  $b$  term was introduced, and finally a sub-regular interaction parameter, until the fit was satisfactory.

The selected phase diagram data of the  $\beta$  phase were the phase boundaries proposed by Sai Baba et al. [39] and Grønvold et al. [40] as well as tie-lines and invariant arrests of Ipsier et al. [30]. The  $\epsilon$  phase was optimized to fit the  $\delta' + \epsilon$  tie-lines and invariant arrests of the preceding paper *Part I*, and of Ipsier et al. [30], with the homogeneity range proposed by Brostigen et al. [41].

## 5.3. $\beta'$ and $\delta$ phases

The  $a$  parameters of the  $\beta'$  and  $\delta$  phase end-members were fitted to the formation enthalpies estimated via DFT. The temperature-dependent  $b$  parameters were then adjusted to obtain reasonable Gibbs energies of the phases. Interaction terms could then be fitted to isopiestic activity data. The interaction and the  $b$  terms of the end-members could then be optimized together, by also including invariant arrests and liquidus data. Parameters in the  $\delta$  phase were manually adjusted to move the resulting miscibility gap to an approximate position, after which the parameters, including the  $a$  terms, were optimized to fit the  $\delta + \delta'$  tie-lines as well as solidus and solvus data.

The  $b$  term of the  $\beta'$ - $Fe_3Te_2$  end-member was manually adjusted to get the phase approximately in place. Both end-member  $b$  terms and interaction parameters were then included in the optimization to fit invariant arrests [30],  $\beta + \beta'$  tie-lines [30] and activity data by Ipsier et al. [6].

The  $\delta$  phase was optimized with the phase boundaries and tie-lines of the experimental *Part I* and of Ipsier et al. [30], together with the evaluated end-member formation energies of  $\delta$ - $FeTe$ ,  $\delta$ - $FeTe_2$ ,  $\delta'$ - $FeTe$  and  $\delta'$ - $FeTe_2$ . The eutectoid  $\delta \rightarrow \beta + \delta'$  was fitted to the temperature found via DTA in the experimental *Part I* (Part I, Fig. 4).

When most phases were in place, the liquid interaction terms were optimized to obtain a better fit of  $\beta'$ ,  $\delta$  and  $\epsilon$  invariant arrests, liquidus and solidus data. It was seen that the  $\epsilon$  phase temperature of formation was underestimated, and the  $a$  term was optimized instead of fixed to the evaluated enthalpy of formation.

## 5.4. $\gamma$ phase

After adjusting the  $\beta$  and  $\delta$  parameters to fit the  $\beta + \delta$  phase boundaries, the  $\gamma$  phase was optimized to fit its invariant temperatures of formation and decomposition. Then an overall optimization was performed of the end-member  $a$  and  $b$  terms, and interaction parameters of all solution phases in order to improve the fit of all invariant reactions to DTA data, especially in the  $\beta' + \gamma + \delta$  region.

## 5.5. Numerical fine-tuning of data and parameters

For the overall optimization including most of the phases, the data were weighted due to differences in published errors, and to prioritize well confirmed data points when compromising was necessary. The relative weights were as the following: low for heat capacity data and very low for isopiestic

activity data. Enthalpy, phase boundary and invariant reaction data were normally weighted, and DFT data slightly lower. Invariant reactions including the  $\gamma$  and  $\delta$  phases as well as the  $\delta + \delta'$  miscibility gap were weighted higher.

After each successful convergence of a phase description, the contribution of parameters to the solution was tested by rescaling the error and controlling the relative standard deviations. Parameters with large standard deviations, usually  $b$  terms in higher-order interaction terms, were removed and the system re-optimized. Thus the set of variables was reduced to the smallest necessary for an overall good fit.

## 6. Results and discussion of DFT calculations

The lattice stability of FCC\_A1 and BCC\_A2 tellurium were evaluated and used in the modeling of Te solubility in the iron terminal phases. The formation energies of the end-members (Table 3) of the  $\beta$ ,  $\beta'$ ,  $\epsilon$ ,  $\delta$  and  $\delta'$  phases are summarized in Table 4 together with converged parameters. Figure 1 displays the formation energies evaluated in this work, with magnification on the  $\delta/\delta'$  region.

In phases of the NiAs-type structure, here  $\delta$  and  $\delta'$ , some atoms may be interstitially dissolved in the trigonal-bipyramidal holes [31]. In order to test the possibility of Fe atoms occupying those sites, the formation energy of the end-member  $\delta'$ - $Fe_2Te$ , i.e.  $(Fe)_1(Fe)_1(Fe)_2(Te)_2$ , with purely hypothetical interstitial iron in the trigonal-bipyramidal sites was evaluated; the highly positive result (Table 4) indicated that it is not a stable configuration, and iron was not added to the third sublattice for the modeling.

As expected, the formation energies of  $\delta$  and  $\delta'$  show that the former, monoclinic configuration is slightly more stable at lower Te content while the latter, hexagonal one is stable at higher Te content (Figure 1); as seen in Table 4, their energies are very close. The triclinic  $P1$  was calculated with lattice parameters equivalent to the monoclinic  $Cc$ , hence the very small difference in energy. The unit cell with space group  $C2/m$  has the composition of 57.14 at% Te, lying within the stability region of the  $\delta$  phase, although the calculation was still made at 0 K. After the lattice parameters were optimized by static calculations, the volume was relaxed followed by a shape relaxation. The  $\beta$  angle drastically changed from about  $90.5^\circ$  to  $85^\circ$ , because the Fe(1) interstitials were offset from the preferred octahedral coordination with surrounding Te atoms, making it dynamically unstable. Subsequently, all degrees of freedom were relaxed, and the Fe(1) atoms moved into the octahedral sites. The cell volume decreased by 5 %, shifted back to  $\beta = 90.65^\circ$  and the formation energy drastically decreased from 12 kJ/mol to 2.62 kJ/mol (Table 4). It also obtained a net zero magnetic moment, in contrast with the other magnetic  $\delta$  and  $\delta'$  phase end-members. While  $C2/m$  has a lower formation energy than  $Cc$  and  $P1$ , they are evaluated at different composition and therefore not directly comparable.

The  $\beta'$  phase was relaxed in the crystal structure of the ternary  $Fe_{0.28}Ni_{0.28}Te_{0.44}$  of the rhombohedral space group 160. The calculated enthalpy of formation is positive as the end-member composition lies outside of the region of stability. However, it is small and the phase is stable only at high temperatures; therefore it should not be ruled out that this is the structure of the  $\beta'$  phase.

Table 4: Relaxed lattice parameters and 0 K formation energies ( $\Delta E$ ) from DFT calculations on Fe-Te end-members.  $\beta$  is only written out if it is not 90°. \*:  $\alpha = \beta = 90.1^\circ$  in triclinic setting equivalent to  $\beta = 90.2^\circ$  in monoclinic setting.

Phase	Energy cutoff [eV]	k-points	Relaxed lattice parameters [ $\text{\AA}$ ]				$\Delta E_f$ [kJ/mol]
			a	b	c	$\beta^\circ$	
$\beta\text{Fe}_2\text{Te}$	510	34x34x21	4.03	-	6.042		10.23
$\beta\text{FeTe}$	510	34x34x21	3.635	-	6.712		-5.20
Exp. $\beta\text{-Fe}_{1.11}\text{Te}$ [42]			3.829		6.288		
$\beta'\text{Fe}_3\text{Te}_2$	450	23x23x4	3.984	-	20.938		0.99
$\delta\text{FeTe}$ P1	470	20x20x14	4.101	-	5.07	90.02	4.90
$\delta\text{FeTe}$ Cc	470	15x8x12	4.105	7.11	5.06	90.05	4.88
$\delta\text{Fe}_3\text{Te}_4$ C2/m	510	9x16x6	6.677	3.85	10.89	90.65	2.62
$\delta\text{FeTe}_2$ P1	470	24x24x14	3.733	-	5.845	90.01	-5.41
Exp. $\delta\text{-Fe}_{0.75}\text{Te}$ [40]			3.846		5.641	90.1*	
$\delta'\text{FeTe}$	550	41x41x27	4.108	-	5.068		5.04
$\delta'\text{FeTe}_2$	510	41x41x27	3.736	-	5.854		-5.50
$\delta'\text{Fe}_2\text{Te}$	630	41x41x27	4.220	-	5.312		47.45
Exp. $\delta'\text{-Fe}_2\text{Te}_3$ [43]			3.813		5.630		
$\epsilon\text{FeTe}_2$	530	24x20x33	5.247	6.242	3.886		-17.2
$\epsilon\text{Te}_2$	510	27x22x36	5.183	7.530	3.115		10.70
Exp. $\epsilon\text{-FeTe}_2$ [41]			5.266	6.268	3.874		
FCC_A1-Te	370	27x27x27	4.832	-	-		39.8
BCC_A2-Te	370	27x27x27	3.846	-	-		29.7

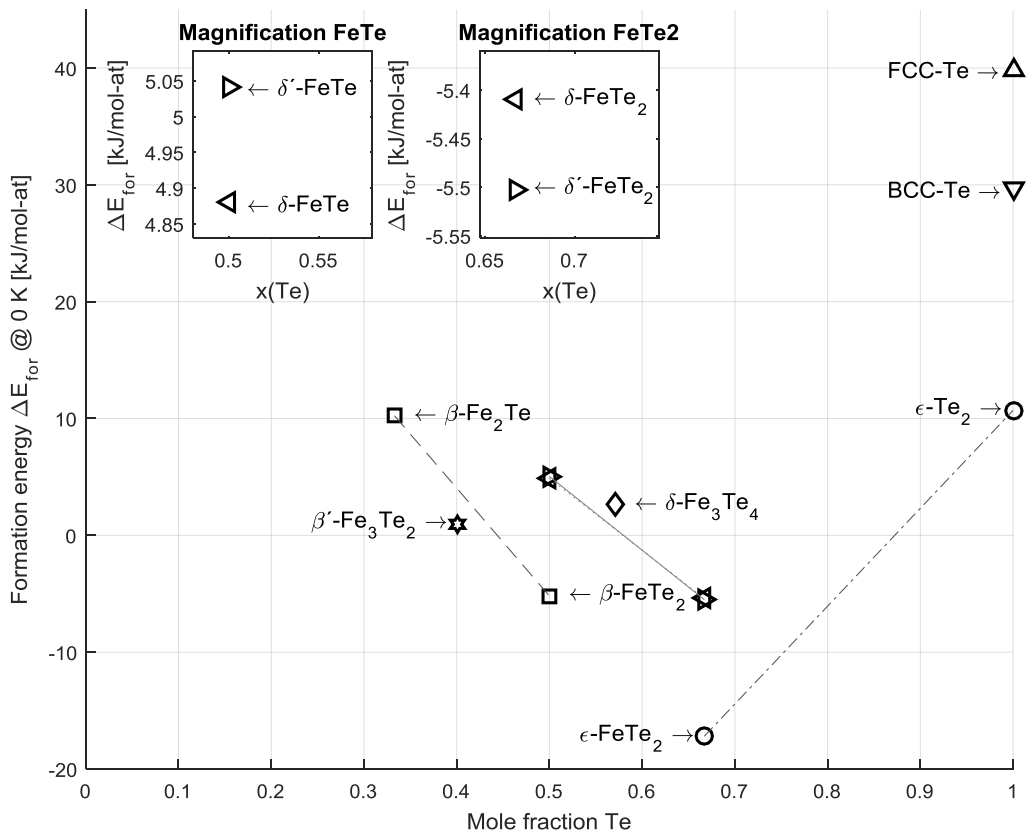


Figure 1: Enthalpy of formation at 0 K relative to BCC\_A1 and A8 reference states for Fe and Te, respectively, evaluated via DFT. Diagram inserts separate the  $\delta$  and  $\delta'$  phases. Lines guide the eyes between end-members of the same phase.

## 7. Results and discussion of thermodynamic assessment

Figure 2 shows the final calculated phase diagram compared with the liquidus data by Ipser et al. [30] and Chiba [38]. Figure 3 is magnified in the region of interest of the intermediate phases, compared with selected experimental data. The different phase regions compared with experimental phase diagram data is discussed in the subsections below, followed by a comparison of thermodynamic data, and finally a comparison of Gibbs energy of formation of iron tellurides with previous predictions.

### 7.1. Liquid and terminal phases

The liquidus of the Fe-Te system (see Figure 2) is entirely consistent with the data of Ipser et al. [30], and that of Chiba [38], excluding the two points that deviate most from the main body of data. As observed in Figure 3, the description also agrees well with the data gathered via DTA in *Part I: Experimental study*, most importantly the iron-rich high-temperature point, consistent with the previously proposed steep liquidus [30], thus supporting the liquid miscibility gap. Although not shown in these figures, no inverted miscibility gap is found up to 6000 K.

The solubility of the  $\alpha$ -Fe phase fits the tie-lines by Ipser et al. and those gathered in *Part I*. The subregular solution parameter optimized to achieve this also resulted in a gamma loop (Figure 2), as Okamoto et al. [44] predicted in their review.

### 7.2. $\beta$ and $\beta'$ phases

In order to fit the  $\beta + \beta'$  boundaries measured in this work, consistent with the tie-lines by Ipser et al. [30], in addition to the  $\beta + \gamma$  boundary data, the phase would require an unnatural shape. The rather strong peak found via DTA of sample FT47\_D (Part I, Fig. 4) indicates that the  $\beta' \rightarrow \beta + \gamma$  invariant extends up to this point, while maintaining consistency with the  $\beta + \beta'$  tie-lines. The present model seems to give a more natural shape of the  $\beta$  phase, than it would have by following all published tie-lines. The phase boundary compositions from isothermal heat treatments in this work are not accurate enough to conclude on data inconsistency.

### 7.3. $\delta/\delta'$ and $\gamma$ phases

The  $\delta$  phase fit within error margins to the selected data, but including the  $\gamma$  phase made it difficult, and compromises were necessary to avoid introducing an unrealistic number of interaction terms. One would either have to elevate the peritectic temperature of  $\delta$  phase formation, incline the  $\delta + \delta'$  miscibility gap, or lower the eutectoid invariant arrests of the phase. All those compromises were assessed, and it was eventually selected to fit the invariant reactions at the expense of the  $\gamma + \delta/\delta$  and  $\delta'/\delta' + \epsilon$  boundaries, since the invariant reactions were more accurately determined via DTA. Since no  $\gamma$  phase composition was found in the isothermal heat treatments, the tie-lines that were intended to be in equilibrium with the  $\gamma$  phase are treated as  $\beta + \delta$  tie-lines. The  $\delta$  phase boundaries fits the experimental data much better when the  $\gamma$  phase is suspended, as shown in the phase diagram of Figure 4.

### 7.4. $\epsilon$ phase

The  $\epsilon$  phase description did not fit well with the evaluated enthalpy of formation together with the peritectic invariant temperature; when the parameters instead were fitted to the phase diagram, the enthalpy of formation coincided very well with the calorimetric measurements by Vladimirova et al. [9] and the  $\epsilon$ -FeTe<sub>2</sub> end-member formation energy evaluated via DFT in this work, as seen in Figure 6. The model is in addition consistent with the  $\epsilon + L$  and  $\delta' + \epsilon$  tie-lines evaluated from samples FT77\_T1 and FT65\_T2.

### 7.5. Thermodynamic activity, chemical potential and heat capacity

Figure 5 presents the calculated tellurium activity with varying composition at 700 °C, relative to the liquid phase, compared with isopiestic [6] and partial pressure data [2,4,5]. Figure 7 and Figure 8 similarly present the calculated chemical potential of iron relative to BCC at 750 and 835 K, respectively, compared with the EMF data by Geiderikh [1]. It proved difficult to fit all activity data sets together. Therefore, all models were optimized to fit the isopiestic activity data by Ipser et al. (Figure 5), since they vary in both temperature and composition, and then compare with the EMF and partial pressure data sets. As can be seen in the figures, the thermodynamic description agrees very well with the isopiestic activity data, and sufficiently well with partial pressure and EMF data.

Figure 9 and Figure 10 show the calculated heat capacity of the  $\epsilon$  and  $\beta$  phases, respectively, and they agree well with selected experimental data. The magnetic transition in the  $\beta$  phase at 67 K was not modeled, and the single point seen in Figure 9 that strongly deviates from the linear behavior was regarded as an artifact and ignored. The heat capacity of the  $\epsilon$  phase (Fig. Figure 10) was only fitted to the work by Westrum et al. [10]. Mikler et al. [11], in their heat capacity measurement on an  $Fe_{0.324}Te_{0.676}$  sample, noted an anomalous increase in  $C_p$  at higher temperature that could be due to precipitation of pure tellurium. Figure 11 shows their measured composition and temperature range relative to the phase diagram; it seems probable that their sample initially contained small amounts of pure tellurium. Figure 12 shows the calculated heat capacity for that composition compared with their data, and indeed it seems possible that a contribution from the tellurium gives rise to an increase in  $C_p$  of such a magnitude.

### 7.6. Application: Predicted formation energy of iron tellurides

The final Gibbs energy models of the Fe-Te system are listed in Table 1 in the Appendix. The  $b \cdot T$  terms in the  $\beta$ - $FeTe$  and the  $\epsilon$ - $FeTe_2$  end-members are notably high. This is because these phases are very stable, as shown by the magnitude of the enthalpy of formation in Figure 6, thus making it necessary to have such large positive values in order to destabilize them at higher temperatures. Table 5 shows calculated Gibbs energy of formation compared with estimated values available in literature, with reasonable agreement. The properties at the Te rich side of the  $\beta$  phase show larger disagreement than the Fe rich side, due to the slightly higher enthalpy of formation from this description. The enthalpy of formation of the  $\epsilon$  phase has a large disagreement from derived data, but the description agrees better with formation enthalpy from DFT and calorimetric data on  $\beta + \epsilon$  samples (see Figure 6) [9].

Table 5: Enthalpies and Gibbs energies of formation of iron tellurides compared with data from literature.

<i>Formula</i>	<i>Phase</i>	<i>Temp. [K]</i>	$\Delta_f^\circ G_m$ [kJ/mol-f.u.] ( <i>Ref. value</i> )	$\Delta_f^\circ H_m$ [kJ/mol-f.u.] ( <i>Ref. value</i> )	<i>Ref.</i>
$FeTe_{0.81}$	$\beta$	298.15	-21.2 (-21.1)	-17.6 (-17.2)	[45]
$FeTe_{0.94}$	$\beta$	298.15	-24.0 (-29.7)	-20.2 (-27.8)	[45]
$FeTe_{0.9}$	$\beta$	298.15		-19.5 (-23.46)	[8]
$Fe_{0.54}Te_{0.46}$	$\beta$	800	-15.6 (-15.86)		[4]
$FeTe_{1.99}^4$	$\epsilon$	298.15	-51.1 (-58.3)	-51.9 (-65.8)	[39]

<sup>4</sup> Here calculated as  $FeTe_2$  since  $FeTe_{1.99}$  is outside the composition range of the sublattice model.

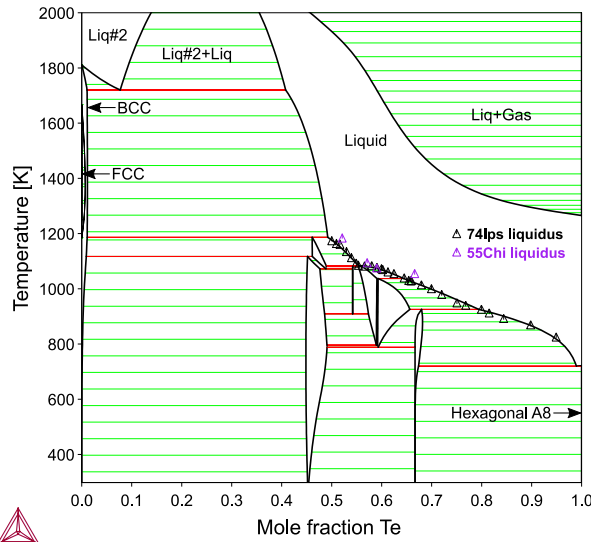


Figure 2: Calculated Fe-Te phase diagram compared with published liquidus data.

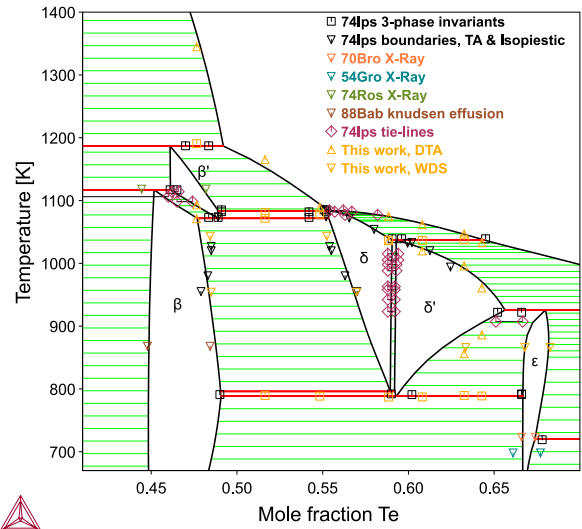


Figure 4: Calculated phase diagram of the same description as Fig. 2, with the  $\gamma$  phase suspended. Note the closer fit of the left solvus of  $\delta$  to experiment.

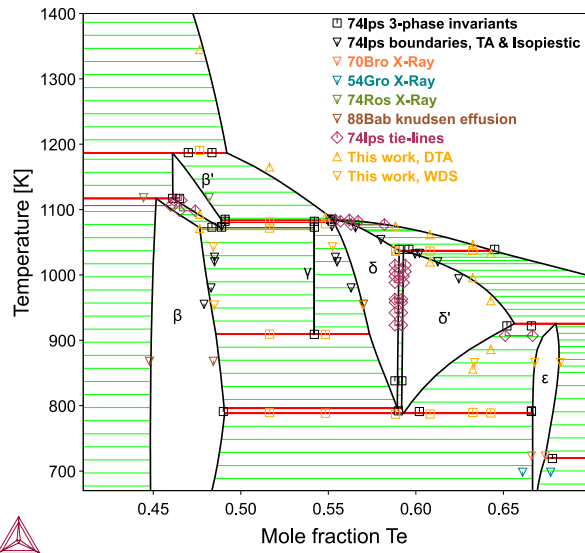


Figure 3: Calculated Fe-Te phase diagram magnified in the region of interest of intermediate phases, compared with selected experimental phase diagram data.

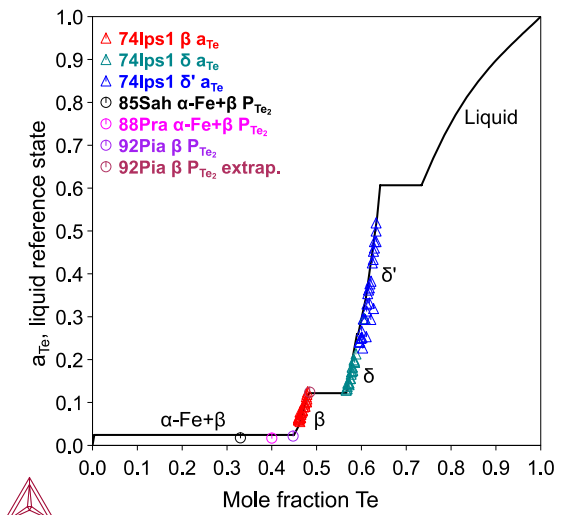


Figure 5: Calculated tellurium activity at 700 °C relative to the liquid phase, of the Fe-Te system compared with experimental data.



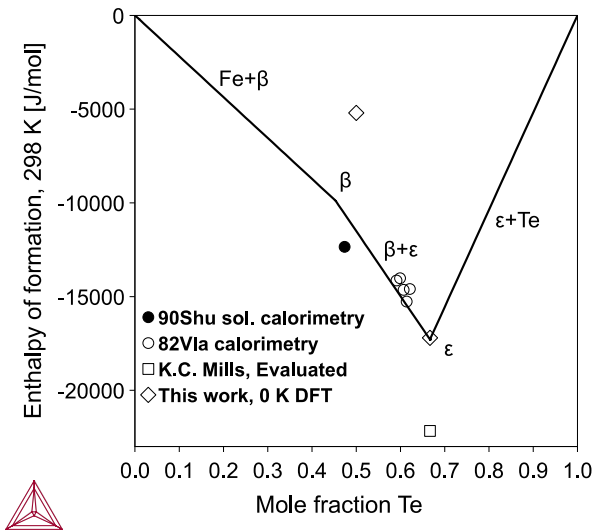


Figure 6: Calculated molar enthalpy of formation of the Fe-Te system at room temperature, compared with published data and DFT data of this work.

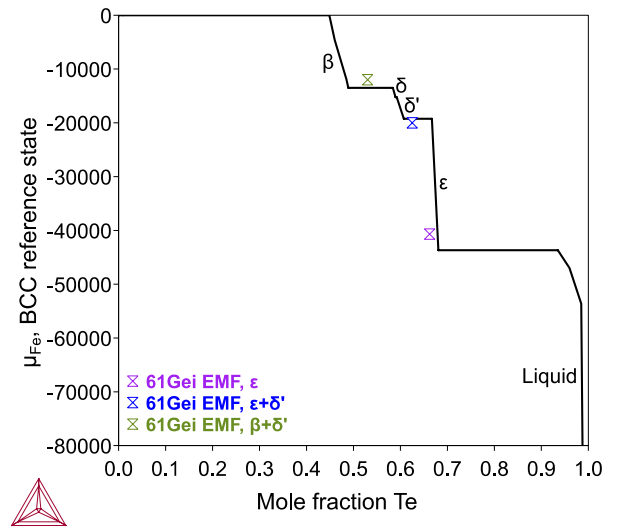


Figure 7: Calculated iron potential, relative to the BCC phase, of the Fe-Te system at 835 K compared with the EMF measurements of Geiderikh et al. [1].

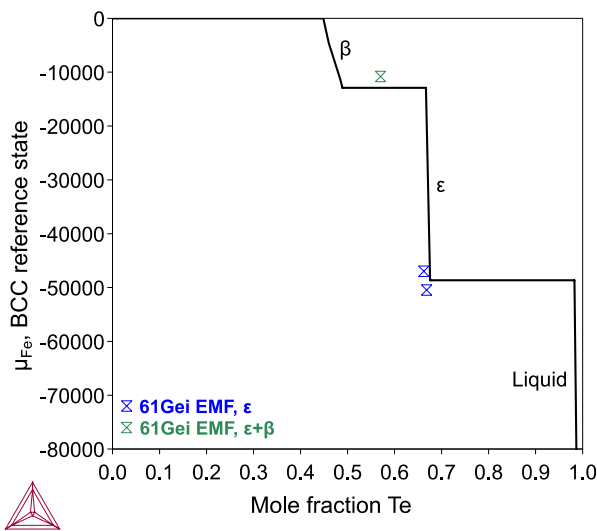


Figure 7: Calculated iron potential, relative to the BCC phase, of the Fe-Te system at 750 K compared with the EMF measurements of Geiderikh et al. [1].

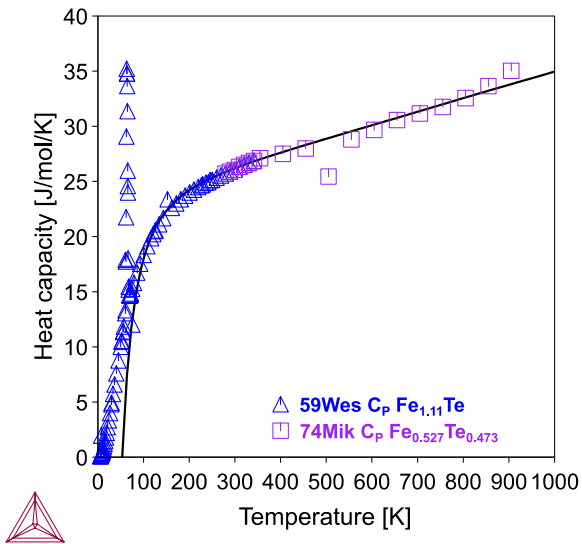


Figure 8: Calculated heat capacity of the  $\beta$  phase compared with experimental data.

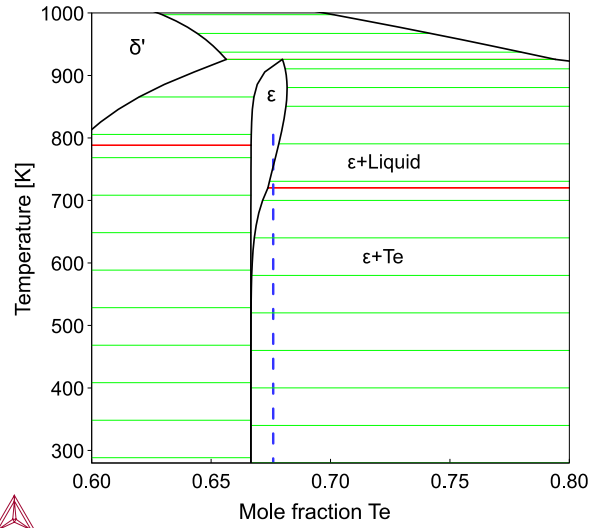


Figure 10: The composition and temperature range of the  $C_p$  measurement of Mikler et al. [11].

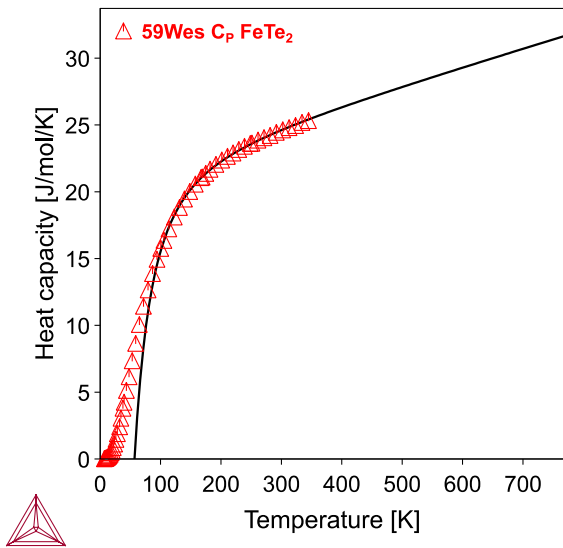


Figure 9: Calculated heat capacity of the  $\epsilon$  phase compared with experimental data.

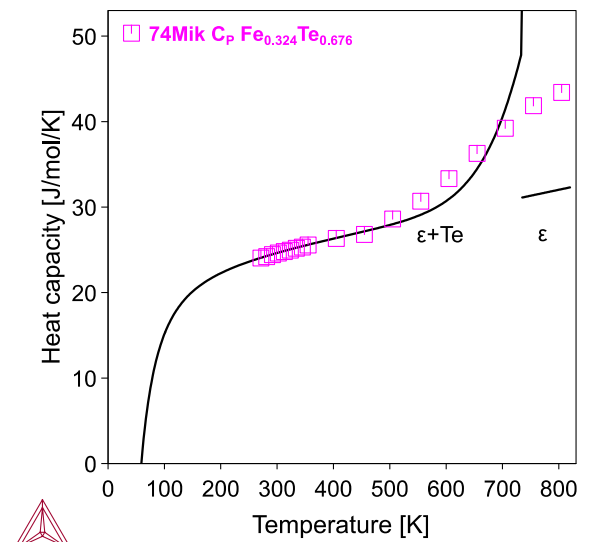


Figure 11:  $C_p$  calculated for the composition in Fig 11, i.e. 0.676 at% Te, compared with the experimental data of Mikler et al. [11].

## 8. Conclusions and future work

In this work a thermodynamic model of the Fe-Te system was developed. The description accurately predicts thermodynamic and phase diagram data available in literature. The  $\delta$  and  $\delta'$  phases were described with a single three-sublattice model separated by a miscibility gap, since they belong to the same structure family, and should experience full solubility in the ternary Fe-Ni-Te system. The design of sublattice models within the Compound Energy Formalism enabled the use of end-member energies of formation estimated via DFT calculations in the optimization. The model may be used both with and without the  $\gamma$  phase: if it is excluded from the phase diagram, the  $\delta$  phase boundary fits experimental data better without negatively affecting other properties. The use of an ionic liquid model with an ordered FeTe associate accommodates for a liquid miscibility gap.

It is recommended to perform a more detailed DFT analysis on the  $\delta$  phase in order to conclude on its space group symmetry. Supercells with random and ordered partial occupation of Fe sites can make the  $Cc$  and  $C2/m$  formation energies more comparable. Finite temperature calculations would enhance the accuracy, as well as indicate if the phase is stabilized by entropy.

The different possible ordered magnetic structures of the  $\beta$  phase are of interest for the semi- and superconductor industries, and the thermodynamic model can be modified to accommodate for this. The proposed model is deemed accurate enough for the purpose of modeling internal fuel pin corrosion in nuclear reactors.

## Acknowledgements

The authors would like to thank the Swedish Research Council (Vetenskapsrådet) for the funding of the project. C.-M. wishes to thank his colleagues at KTH and CEA for the advice in thermodynamic modeling: Drs Bonnie Lindahl and Nathalie Dupin for advice on the modeling, and Prof. Andrei Ruban for lending his advice on the DFT calculations.

C.-M. wishes to thank Prof. Herbert Ipser for the discussions they have had regarding the modelling of the  $\delta$  phases of the Fe-Te system, and especially for personally lending him a copy of his thesis on the system.

Last but not least, C.-M. extends thanks to the components of Nomad Chemistry for advice and support during his work.

## Bibliography

- [1] V. A. Geiderikh, Y. I. Gerasimov och A. V. Nikol'skaya, "Thermodynamic Properties of Iron-Tellurium Alloys in the Solid State," (*TR*) *Proceedings of the Academy of Sciences of the USSR. Physical Chemistry section.*, vol. 137, pp. 394-351, 1961.
- [2] B. Saha, R. Viswanathan, M. Sai Baba, D. Darwin Albert Raj, R. Balasubramanian, D. Karunasagar och C. K. Mathews, "High-temperature mass-spectrometric studies of Te(s) and FeTe<sub>0.9</sub>(s)," *Journal of Nuclear Materials*, vol. 130, pp. 316-325, 1985.
- [3] M. Sai Baba, R. Viswanathan, R. Balasubramanian, D. Darwin Albert Raj, B. Saha och C. K. Mathews, "Vaporization thermodynamics of (iron+tellurium): a high-temperature mass-spectrometric study," *Journal of Chemical Thermodynamics*, pp. 1157-1173, 1988.
- [4] R. Prasad, S. Mohapatra, V. S. Iyer, Z. Singh, V. Venugopal och D. D. Sood, "Thermodynamics of iron telluride (Fe<sub>0.540</sub>Te<sub>0.460</sub>)," *Journal of Chemical Thermodynamics*, vol. 20, pp. 453-456, 1988.
- [5] V. Piacente och P. Scardala, "Study of the vaporization behaviour of iron monotelluride," *Journal of Alloys and Compounds*, vol. 184, pp. 285-295, 1992.
- [6] H. Ipser och K. L. Komarek, "Thermodynamic Properties of Iron-Tellurium Alloys," *Monatshefte für Chemie*, vol. 105, pp. 1344-1361, 1974.
- [7] C. Fabre, "heats of Formation of Some Telluride Crystals," *Comptes Rendus Chimie*, vol. 105, pp. 277-280, 1887.
- [8] N. K. Shukla, R. Prasad, K. N. Roy och D. D. Sood, "Standard molar enthalpies of formation at the temperature 298.15 K of iron telluride (FeTe<sub>0.9</sub>) and of nickel telluride (Ni<sub>0.595</sub>Te<sub>0.405</sub>)," *Journal of Chemical Thermodynamics*, vol. 22, pp. 899-903, 1990.
- [9] V. A. Vladimirova, R. A. Zvinchuk, M. P. Morozova och O. Y. Pakrativa, "Enthalpy of Formation and Structure of Non-stoichiometric Iron Telluride," *Tr: Russian Journal of Physical Chemistry*, vol. 53, nr 3, pp. 346-348, 1982.
- [10] E. F. Westrum, C. Chou och F. Grønvold, "Heat Capacities and Thermodynamic Properties of the Iron Tellurides Fe<sub>1.11</sub>Te and FeTe<sub>2</sub> from 5 to 350 K," *The Journal of Chemical Physics*, vol. 30, nr 3, pp. 761-764, 1959.
- [11] J. Mikler, H. Ipser och K. L. Komarek, "Spezifische Wärmen von FeTe und FeTe<sub>2</sub> von Raumtemperatur bis 900 K," *Monatshefte für Chemie*, vol. 105, pp. 977-986, 1974.
- [12] A. Mani, J. Janaki, T. Geetha Kumary, N. Thirumurugan, S. Kalavathi och A. Bharathi, "Specific heat studies on pristine and oxygenated iron tellurides," *Solid State Communications*, vol. 151, pp. 1210-1213, 2011.
- [13] T. Maekawa och T. Yokokawa, "Enthalpies of infinitely dilute solutions of transition metals in liquid tellurium," *Journal of Chemical Thermodynamics*, vol. 7, pp. 505-506, 1975.
- [14] D. D. Wagman, W. H. Evans, V. B. Parker, R. H. Schumm, I. Halow, S. M. Bailey, K. L. Churney och R. L. Nuttal, "The NBS tables of chemical thermodynamic properties," *Journal of Physical and*

*Chemical Reference Data*, vol. 11, 1982.

- [15] Y. V. Rumyantsev, G. M. Zhiteneva och F. M. Bolondz, "Thermal Stability of Selenides and Tellurides of Iron and Nickel," *Tr. Vost. Sibirisk Filialia, Akad. Nauk SSSR*, vol. 42, p. 114, 1962.
- [16] P. E. Blochl, "Projector augmented-wave method," *Physical Review B*, vol. 50, p. 17953, 1994.
- [17] G. Kresse och D. Joubert, "From ultrasoft pseudopotentials to the projector augmented-wave method," *Physical Review B*, vol. 59, p. 1758, 1999.
- [18] G. Kresse och J. Hafner, "Ab initio molecular dynamics for liquid metals," *Physical Review B*, vol. 47, p. 558, 1993.
- [19] G. Kresse och J. Hafner, "Ab initio molecular-dynamics simulation of the liquid-metal-amorphous-semiconductor transition in germanium," *Physical Review B*, vol. 49, p. 14251, 1994.
- [20] G. Kresse och J. Furthmüller, "Efficiency of ab-initio total energy calculations for metals and semiconductors using a plane-wave basis set," *Computational Materials Science*, vol. 6, p. 15, 1996.
- [21] G. Kresse och J. Furthmüller, "Efficient iterative schemes for ab initio total-energy calculations using a plane-wave basis set," *Physical Review B*, vol. 54, p. 11169, 1996.
- [22] J. P. Perdew, K. Burke och M. Ernzerhof, "Generalized gradient approximation made simple," *Physical Review Letters*, vol. 77, p. 3865, 1996.
- [23] J. P. perdew, K. Burke och M. Ernzerhof, "Erratum: Generalized gradient approximation made simple," *Physical Review Letters*, vol. 78, p. 1396, 1997.
- [24] P. Beiss, "Iron and steel: Manufacturing route," i *Landolt-Börnstein - Group VIII Advanced Materials and Technologies 2A1*, P. Beiss, H. Ruthardt och H. Warlimont, Red., Berlin, Springer-Verlag, 2003, pp. 5.1-5.20.
- [25] SpringerMaterials, "Tellurium (Te) elastic moduli," i *Landolt-Börnstein - Group III Condensed Matter 41C*, U. R. M. S. O. Madelung, Red., Berlin, Springer-Verlag, 1998, p. Online Document 1279.
- [26] M. Hillert, "The compound energy formalism," *Journal of Alloys and Compounds*, vol. 320, pp. 161-176, 2001.
- [27] H. L. Lukas, S. G. Fries och B. Sundman, *Computational Thermodynamics. The Calphad Method.*, New York: Cambridge University Press, 2007.
- [28] E. E. Rodriguez, C. Stock, P. Zajdel, K. L. Krycka, C. F. Majkrzak, P. Zavalij och M. A. Green, "Magnetic-crystallographic phase diagram of the superconducting parent compound  $\text{Fe}_{1+x}\text{Te}$ ," *Physical Review B*, vol. 84, p. 064403, 2011.
- [29] G. Åkesson och E. Røst, "The Crystal Structure of  $\text{Fe}_{.28}\text{Ni}_{.28}\text{Te}_{.44}$ ," *Acta Chemica Scandinavica*, vol. 27, pp. 79-84, 1973.
- [30] H. Ipser, K. L. Komarek och H. Mikler, "Transition Metal-Chalcogen Systems, V.: The iron-

- Tellurium Phase Diagram," *Monatshefte für Chemie*, vol. 105, pp. 1322-1334, 1974.
- [31] I. Jandl, H. Ipser och K. W. Richter, "Thermodynamic modelling of the general NiAs-type structure: A study of first principle energies of formation for binary Ni-containing B8 compounds," *CALPHAD: Computer Coupling of Phase Diagrams and Thermochemistry*, vol. 50, pp. 174-181, 2015.
- [32] M. Hillert, B. Jansson, B. Sundman och J. Ågren, "A two-sublattice model for molten solutions with different tendency for ionization," *Metallurgical Transactions A*, vol. 16, nr 1, pp. 261-266, 1985.
- [33] A. V. Davydov, M. H. Rand och B. B. Argent, "Review of Heat Capacity Data for Tellurium," *Calphad*, vol. 19, nr 3, pp. 375-387, 1995.
- [34] B. Cheynet, P.-Y. Chevalier och E. Fischer, "Thermosuite," *Calphad*, vol. 26, nr 2, pp. 167-174, 2002.
- [35] G. V. Belov, V. S. Iorish och V. S. Yungman, "IVTANTHERMO for Windows - Database on Thermodynamic Properties and Related Software," *Calphad*, vol. 23, nr 2, pp. 173-180, 1999.
- [36] A. T. Dinsdale, "SGTE data for pure elements," *CALPHAD*, vol. 15, nr 4, pp. 317-425, 1991.
- [37] J. O. Andersson, T. Helander, L. Höglund, P. F. Shi och B. Sundman, "Thermo-Calc and DICTRA, Computational tools for materials science," *Calphad*, vol. 26, pp. 273-312, 2002.
- [38] S. Chiba, "The Magnetic Properties and Phase Diagram of Iron Tellurium System," *Journal of the Physical Society of Japan*, vol. 10, nr 10, pp. 837-842, 1955.
- [39] M. Sai Baba, R. Viswanathan och C. K. Mathews, "Thermodynamic and Phase Diagram Studies on Metal-Tellurium Systems Employing Knudsen Effusion Mass Spectrometry," *Rapid communications in mass spectrometry*, vol. 10, pp. 691-698, 1996.
- [40] F. Grønvold, H. Haraldsen och J. Vihovde, "Phase and Structural Relations in the System Iron Tellurium," *Acta Chemica Scandinavica*, vol. 8, pp. 1927-1942, 1954.
- [41] G. Brostigen och A. Kjekshus, "Compounds with the Marcasite Type Crystal Structure V. The crystal structure of FeS<sub>2</sub>, FeTe<sub>2</sub> and CoTe<sub>2</sub>," *Acta Chemica Scandinavica*, vol. 24, nr 6, pp. 1925-1940, 1970.
- [42] J. Leciejewicz, "A Neutron Diffraction Study of Magnetic Ordering in Iron Telluride," *Acta Chemica Scandinavica*, vol. 17, pp. 2593-2599, 1963.
- [43] J. B. Ward och V. H. McCann, "On the <sup>57</sup>Fe Mössbauer spectra of FeTe and Fe<sub>2</sub>Te<sub>3</sub>," *Journal of Physics C: Solid State Physics*, vol. 12, pp. 873-879, 1979.
- [44] H. Okamoto och L. E. Tanner, "The Fe-Te (Iron-Tellurium) System," *Bulletin of Alloy Phase Diagrams*, vol. 11, nr 4, pp. 371-376, 1990.
- [45] C. K. Mathews, "Thermochemistry of transition metal tellurides of interest in nuclear technology," *Journal of Nuclear Materials*, vol. 201, pp. 99-107, 1993.

- [46] G. S. Mann och L. H. Van Vlack, "Fe<sub>1.2</sub>Te-MnTe Phase Relationships in the Presence of Excess Iron," *Metallurgical Transactions B*, vol. 8B, pp. 53-57, 1977.
- [47] H. Kopp, "Investigations of the Specific Heat of Solid Bodies," *Philosophical Transactions of the Royal Society of London*, vol. 155, pp. 71-202, 1865.
- [48] C. Adenis, V. Langer och O. Lindqvist, "Reinvestigation of the Structure of Tellurium," *Acta Crystallographica*, vol. C45, pp. 941-942, 1989.

## Appendix

Table 1: Sublattice models, with corresponding Wyckoff positions, used in the assessment of the Fe-Te system are presented with the resulting converged thermodynamic parameters. GLIQFE, GLIQTE, GHSERFE and GHSERTE are pure element thermodynamic functions from the SGTE PURE5 database [33-36].

Liquid: $(\text{Fe}^{+2})_p(\text{Va}^{\text{Q}}, \text{FeTe}^0, \text{Te}^0)_q$	
${}^\circ G_{\text{Fe}^{+2}} = \text{GLIQFE}$	${}^0 L_{\text{Fe}^{+2}, \text{Va}, \text{FeTe}} = 28248$
${}^\circ G_{\text{Te}} = \text{GLIQTE}$	${}^1 L_{\text{Fe}^{+2}, \text{Va}, \text{FeTe}} = 11391$
${}^\circ G_{\text{FeTe}^0} = -30530 + \text{GLIQFE} + \text{GLIQTE}$	${}^0 L_{\text{Fe}^{+2}, \text{FeTe}, \text{Te}} = -5547$
${}^0 L_{\text{Fe}^{+2}, \text{Va}, \text{Te}} = 50 \cdot T$	${}^1 L_{\text{Fe}^{+2}, \text{FeTe}, \text{Te}} = 345$
	${}^2 L_{\text{Fe}^{+2}, \text{FeTe}, \text{Te}} = 3844$
$\beta'$ : $(\text{Fe}, \text{Va})_3(\text{Te})_2$	Wyckoff: $(3a)_3(3a)_2$
${}^\circ G_{\text{Fe}_3\text{Te}_2} = -30174 - 31.442 \cdot T + 3 \cdot \text{GHSERFE}$	${}^0 L_{\text{Fe}, \text{Va}: \text{Te}} = -70216$
$+ 2 \cdot \text{GHSERTE}$	${}^1 L_{\text{Fe}, \text{Va}: \text{Te}} = -20305$
${}^\circ G_{\text{Te}_2} = 2 \cdot \text{GHSERTE}$	
$\beta$ : $(\text{Fe})_1(\text{Te})_1(\text{Fe}, \text{Va})_1$	Wyckoff: $(2a)(2c)(2c)$
${}^\circ G_{\text{Fe}_2\text{Te}} = 30715 + 2 \cdot \text{GHSERFE} + \text{GHSERTE}$	${}^0 L_{\text{Fe}: \text{Te}: \text{Fe}, \text{Va}} = -118966 + 19.997 \cdot T$
${}^\circ G_{\text{FeTe}} = -36525 + 230.496 \cdot T - 46.536 \cdot T \cdot \ln(T) - 0.01223 \cdot T^2 + 43100 \cdot T^{-1}$	${}^1 L_{\text{Fe}: \text{Te}: \text{Fe}, \text{Va}} = -46154$
$\delta$ and $\delta'$ : $(\text{Fe}, \text{Va})_1(\text{Fe}, \text{Va})_1(\text{Te})_2$	Wyckoff: $(1a)(1b)(2d)$
${}^\circ G_{\text{Fe}_2\text{Te}_2} = -15417 - 47.631 \cdot T + 2 \cdot \text{GHSERFE}$	${}^\circ G_{\text{Te}_2} = 13547 + 2 \cdot \text{GHSERTE}$
$+ 2 \cdot \text{GHSERTE}$	${}^0 L_{\text{Fe}, \text{Va}: \text{Fe}: \text{Te}} = -55623 + 48.634 \cdot T$
${}^\circ G_{\text{VaFeTe}_2} = -30222 - 21.517 \cdot T + \text{GHSERFE}$	${}^1 L_{\text{Fe}, \text{Va}: \text{Fe}: \text{Te}} = -3328$
$+ 2 \cdot \text{GHSERTE}$	${}^0 L_{\text{Fe}: \text{Fe}, \text{Va}: \text{Te}} = -56003 + 48.551 \cdot T$
${}^\circ G_{\text{FeVaTe}_2} = -30222 - 21.517 \cdot T + \text{GHSERFE}$	${}^1 L_{\text{Fe}: \text{Fe}, \text{Va}: \text{Te}} = -5291$
$+ 2 \cdot \text{GHSERTE}$	
$\epsilon$ : $(\text{Fe}, \text{Va})_1(\text{Te})_2$	Wyckoff: $(2a)(4g)$
${}^\circ G_{\text{FeTe}_2} = -73469 + 318.524 \cdot T - 63.9656 \cdot T \cdot \ln(T) - 0.020402 \cdot T^2 + 107200 \cdot T^{-1}$	${}^\circ G_{\text{Te}_2} = 10700 + 2 \cdot \text{GHSERTE}$
	${}^0 L_{\text{Fe}, \text{Va}: \text{Te}} = 62432 - 71.949 \cdot T$
$\gamma$ : $(\text{Fe})_1(\text{Te})_{1.183}$	
${}^\circ G_{\text{FeTe}_{1.183}} = -23492 - 17.005 \cdot T + \text{GHSERFE} + 1.183 \cdot \text{GHSERTE}$	
BCC_A2: $(\text{Fe}, \text{Te})_1(\text{Va})_3$	Wyckoff: $(2a)(6b)$
${}^\circ G_{\text{Te}} = 25600 + \text{GHSERTE}$	${}^0 L_{\text{Fe}, \text{Te}: \text{Va}} = -22594$
FCC_A1: $(\text{Fe}, \text{Te})_1(\text{Va})_1$	Wyckoff: $(4a)(4b)$
${}^\circ G_{\text{Te}} = 35700 + \text{GHSERTE}$	



Table 2: Table of invariant equilibria calculated from the thermodynamic model in the present work, compared with the phase diagram review by Okamoto and Tanner [44].

Reaction	at.% Te	T [°C]	Ref. T [°C] [44]	Reaction type
$L \leftrightarrow \delta Fe$	0	1537.8	1538	Melting
$\delta Fe \leftrightarrow \gamma Fe$	0	1394.3	1394	Allotropic
$\gamma Fe \leftrightarrow \alpha Fe$	0	911.7	912	Allotropic
$L\#2 \leftrightarrow L\#1 + \alpha Fe$	7.70	1447.1	~1500 [46]	Monotectic
$L + \alpha Fe \leftrightarrow \beta'$	46.10	913.5	914	Peritectic
$\alpha Fe + \beta' \leftrightarrow \beta$	45.17	843.9	844	Peritectoid
$\beta' + L \leftrightarrow \delta$	55.30	810.6	812	Peritectic
$\beta' + \delta \leftrightarrow \gamma$	54.19	807.3	809	Peritectoid
$\beta' \leftrightarrow \gamma + \beta$	48.86	799.1	800	Eutectoid
$\gamma \leftrightarrow \beta + \delta$	54.19	636.3	636	Eutectoid
$\delta \leftrightarrow \beta + \delta'$	58.94	522.9	565±15 [30]	Eutectoid
$\delta' \leftrightarrow \beta + \epsilon$	59.30	515.3	519	Eutectoid
$\delta + L \leftrightarrow \delta'$	59.28	764.0	766	Peritectic
$\delta' + L \leftrightarrow \epsilon$	67.98	652.5	649	Peritectic
$L \leftrightarrow \epsilon + Te$	98.96	446.9	448	Eutectic
$L \leftrightarrow Te$	100	449.5	449.57	Melting